1-1-2015

Metabolic and photosynthetic consequences of blocking starch biosynthesis in the green alga Chlamydomonas reinhardtii sta6 mutant

Anagha Krishnan
Waksman Institute of Microbiology

G. Kenchappa Kumaraswamy
Waksman Institute of Microbiology

David J. Vinyard
Waksman Institute of Microbiology

Huiya Gu
Colorado School of Mines

Gennady Ananyev
Rutgers University–New Brunswick

See next page for additional authors

Recommended Citation

Krishnan, A., Kumaraswamy, G., Vinyard, D., Gu, H., Ananyev, G., Posewitz, M., & Dismukes, G. (2015). Metabolic and photosynthetic consequences of blocking starch biosynthesis in the green alga Chlamydomonas reinhardtii sta6 mutant. *Plant Journal, 81* (6), 947-960. https://doi.org/10.1111/tpj.12783

the plant journal

SEB Society for Experimental Biology

The Plant Journal (2015) **81,** 947–960 doi: 10.1111/tpj.12783

Metabolic and photosynthetic consequences of blocking starch biosynthesis in the green alga *Chlamydomonas reinhardtii sta6* mutant

Anagha Krishnan[1], G. Kenchappa Kumaraswamy[1], David J. Vinyard[1,2,†], Huiya Gu[3], Gennady Ananyev[2], Matthew C. Posewitz[3] and G. Charles Dismukes[1,2,*]

[1]*Waksman Institute of Microbiology, Rutgers: The State University of New Jersey, Piscataway, NJ 08854, USA,*
[2]*Department of Chemistry & Chemical Biology, Rutgers: The State University of New Jersey, Piscataway, NJ 08854, USA, and*
[3]*Department of Chemistry and Geochemistry, Colorado School of Mines, Golden, CO 80401, USA*

Received 25 November 2014; revised 20 January 2015; accepted 21 January 2015; published online 3 February 2015.
*For correspondence (e-mail dismukes@rci.rutgers.edu).
†Present address: Department of Chemistry, Yale University, New Haven, CT 06520, USA.

SUMMARY

Upon nutrient deprivation, microalgae partition photosynthate into starch and lipids at the expense of protein synthesis and growth. We investigated the role of starch biosynthesis with respect to photosynthetic growth and carbon partitioning in the *Chlamydomonas reinhardtii* starchless mutant, *sta6*, which lacks ADP-glucose pyrophosphorylase. This mutant is unable to convert glucose-1–phosphate to ADP-glucose, the precursor of starch biosynthesis. During nutrient-replete culturing, *sta6* does not re-direct metabolism to make more proteins or lipids, and accumulates 20% less biomass. The underlying molecular basis for the decreased biomass phenotype was identified using LC–MS metabolomics studies and flux methods. Above a threshold light intensity, photosynthetic electron transport rates (water → CO_2) decrease in *sta6* due to attenuated rates of NADPH re-oxidation, without affecting photosystems I or II (no change in isolated photosynthetic electron transport). We observed large accumulations of carbon metabolites that are precursors for the biosynthesis of lipids, amino acids and sugars/starch, indicating system-wide consequences of slower NADPH re-oxidation. Attenuated carbon fixation resulted in imbalances in both redox and adenylate energy. The pool sizes of both pyridine and adenylate nucleotides in *sta6* increased substantially to compensate for the slower rate of turnover. Mitochondrial respiration partially relieved the reductant stress; however, prolonged high-light exposure caused accelerated photoinhibition. Thus, starch biosynthesis in *Chlamydomonas* plays a critical role as a principal carbon sink influencing cellular energy balance however, disrupting starch biosynthesis does not redirect resources to other bioproducts (lipids or proteins) during nutrient-replete culturing, resulting in cells that are susceptible to photochemical damage caused by redox stress.

Keywords: *Chlamydomonas reinhardtii*, *sta6*, photosynthetic electron transport chain, oxygen evolution rate, CBB cycle, malonyl CoA, NADPH re-oxidation.

INTRODUCTION

Microalgal strains partition photosynthetically fixed carbon into terminal products for biosynthesis and storage, including proteins, lipids and starch, in amounts that vary appreciably by genus, species and culturing conditions (Benamotz *et al.*, 1985; Becker, 1994; Subramanian *et al.*, 2013). Together with growth rate and tolerance to environmental stresses, these traits determine their suitability for biotechnological applications. The search for natural strains that accumulate desired products has been augmented by genetic approaches that aim to create transgenic lines that are better suited with respect to one or more of these desired traits. For example, in *Chlamydomonas reinhardtii* (Chlorophyceae; referred to as *Chlamydomonas* throughout), genetically blocking alternative competing pathways, including starch biosynthesis, increased lipid content by two- to eightfold relative to control strains in N-deficient media (Wang *et al.*, 2009; Li *et al.*, 2010a,b; Radakovits *et al.*, 2010; Work *et al.*, 2010). The most widely characterized *Chlamydomonas* starchless mutant, *sta6*, contains a deletion in the small subunit of

ADP-glucose pyrophosphorylase (AGPase), which results in higher lipid production, and this mutant has been extensively investigated (Wang *et al.*, 2009; Li *et al.*, 2010a, b; Work *et al.*, 2010; Goodson *et al.*, 2011; Siaut *et al.*, 2011; Fan *et al.*, 2012; Blaby *et al.*, 2013). It was found that, following growth of *sta6*, removal of all nitrogen and addition of acetate to the medium led to cells so engorged with lipids that they floated to the surface (Goodson *et al.*, 2011; Goodenough *et al.*, 2014). However, *sta6* cells have been reported to display decreased photosynthetic activity compared to wild-type cells under some autotrophic and mixotrophic conditions (Li *et al.*, 2010a; Work *et al.*, 2010). Notably, *sta6* displayed an altered energy partitioning at photosystem II (PSII), and a reduced photochemical yield that was attributed to lower F_v'/F_m' (a chlorophyll fluorescence parameter representing the maximum quantum efficiency of PSII photochemistry under continuous illumination) and *qP* (approximating the proportion of PSII reaction centers that are open under a given light intensity) relative to the reference strains (Li *et al.*, 2010b), indicating that the starchless phenotype exhibits consequences as far upstream as water oxidation by PSII. The reduced levels of water oxidation and CO_2 fixation in *sta6* renders this strain undesirable from an overall bioenergy perspective. To date, identification of metabolic bottlenecks induced by the absence of starch accumulation, and precise mapping of photosynthetic electron transport (PET) chain alterations in *sta6*, have not been performed; such aspects are explored in the present study.

Deletion of AGPase in *sta6* eliminates the conversion of glucose-1–phosphate to ADP-glucose, the activated substrate used in covalent glucose linkage reactions. In the majority of prokaryotes, AGPase is a homotetrameric protein, but it is a heteromeric enzyme in eukaryotes (Ballicora *et al.*, 2004), with separate small and large subunits. However, in both cases, AGPase targets glucose for incorporation into carbon and energy storage polysaccharides. In Arabidopsis, deletion of the small subunit of AGPase led to a 33% reduction in photosynthetic O_2 evolution, while loss of the large subunit resulted in a moderate decrease of 8% (Sun *et al.*, 1999). Similarly, in cyanobacterial mutants lacking AGPase, photosynthetic O_2 evolution is highly inhibited (Suzuki *et al.*, 2010; Grundel *et al.*, 2012), indicating the importance of AGPase activity not only for producing starch/glycogen but also for maintaining photosynthetic activities by providing photosynthetic ATP and NADPH sinks.

Here, we have used a highly quantitative metabolomics approach to determine changes in the intracellular pool sizes of key metabolites, adenylate energy charge, and pyridine nucleotide redox poise. We combine this approach with measurements of proteins, lipids, carbohydrates, biomass and PET to identify the metabolic and photosynthetic bottlenecks in the production of energy carriers and carbon precursors for starch and lipid biosynthesis in *sta6* and the starch-accumulating control strain *cw15.*

RESULTS

Photoautotrophic growth and biomass accumulation

Figure 1(a) compares *sta6* and *cw15* growth rates in photoautotrophic HS medium (see Experimental procedures) supplemented with 5 mM $NaHCO_3$, illuminated using white light (100 μE m^{-2} sec^{-1}). The *sta6* mutant grew more slowly relative to *cw15*, with a doubling time that was approximately 30% longer ($P = 0.03$). Both strains reached stationary phase simultaneously, but *sta6* had an approximately one-third lower cell density relative to the control strain. As the cultures grew, the light penetration decreased because of self-shading, with transmitted intensity dropping to as low as 25 μE m^{-2} sec^{-1} in stationary phase cultures.

At stationary phase (after 96 h of growth), the three major biochemical fractions (total reducing carbohydrate, lipids and proteins) were quantified in *sta6* and *cw15* (Figure 1b and Table 1). In addition, we also measured the biomass distribution in two other starch-synthesizing reference strains (CC124 and D66) to assess biomass distribution across multiple control strains. The dry cell weights of the *sta6* mutant cultures were approximately 20–35%

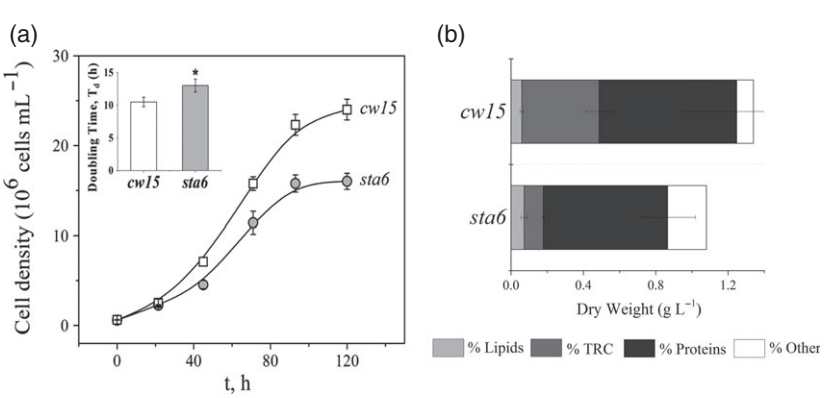

Figure 1. Photoautotrophic growth and biomass.
(a) Photoautotrophic growth phenotypes for *cw15* and *sta6*. The inset shows the doubling time based on fits to Gompertz curves. The asterisk indicates a statistically significant difference compared with *cw15* ($P < 0.05$).
(b) Biomass composition of *cw15* and *sta6* under N-replete, photoautotrophic conditions measured after 4 days of growth. The *y* axis represents the dry weight in grams. Values are means and standard errors of three biological replicates.

Table 1 Biomass composition of *sta6* and three reference strains, *cw15*, CC124 and D66, under NH_4Cl-replete photoautotrophic culturing conditions

	sta6	*cw15*	CC124	D66
DW (0 h)	0.13 ± 0.04	0.07 ± 0.00	0.18 ± 0.03	0.12 ± 0.04
DW (96 h)	1.08 ± 0.05	1.34 ± 0.13	1.29 ± 0.11	1.49 ± 0.06
DW flux (g l^{-1} d^{-1})	0.23 ± 0.02	0.32 ± 0.02	0.27 ± 0.02	0.34 ± 0.03
Lipid (96 h)	0.072 ± 0.016	0.059 ± 0.010	0.106 ± 0.008	0.109 ± 0.023
% Lipid	6.6 ± 1.2	4.4 ± 0.3	8.3 ± 1.2	7.3 ± 1.5
TRC(96 h)	0.106 ± 0.006	0.428 ± 0.072	0.246 ± 0.029	0.493 ± 0.142
% TRC	9.88 ± 0.14	31.8 ± 2.4	19.1 ± 1.2	33.0 ± 8.8
Protein (96 h)	0.688 ± 0.153	0.761 ± 0.293	0.645 ± 0.109	0.702 ± 0.083
% Protein	62.4 ± 18.0	56.1 ± 16.5	49.9 ± 7.2	47.5 ± 7.3
Mass balance	80.5 ± 16.3	92.2 ± 19.2	77.2 ± 8.7	87.8 ± 6.0

Values are reported as g l^{-1}, and values are means ± SD for three independent biological replicates.

lower than the dry cell weights of all three reference strains. The total reducing carbohydrate (TRC) content in *sta6* was between two and five times lower than that in the control strains. Additionally, *sta6* has a slightly increased protein content relative to D66 and CC124; however, this is not statistically different when compared to *cw15*.

These results indicate that loss of starch biosynthesis does not result in the repartitioning of carbon from TRC to lipids and proteins under nutrient-replete conditions; instead cellular biomass is reduced by a degree that is similar to the reduction in TRC levels in *sta6* relative to the control strains. The decreased biomass accumulation implies that a primary adaptation in this starchless mutant is decreased/altered photosynthetic electron transport.

Photosynthetic oxygen evolution rate, PSII quantum yield of charge separation, and electron transport rate

To quantify the effect of a lack of starch biosynthesis on photosynthesis, photosynthetic O_2 evolution rates (OERs) were measured for *sta6* and *cw15* using a Clark electrode after illumination with a range of light intensities (λ_{max} = 620 nm). At light levels up to 60 μE m^{-2} sec^{-1}, *sta6* and *cw15* have comparable OER, but as the light intensity increased above this threshold, the differences between *cw15* and *sta6* increased, and at a light intensity of 680 μE m^{-2} sec^{-1}, *sta6* shows a 3.5-fold lower OER than *cw15* (Figure 2a). It important to note that cultures were grown using white light at 60–80 μE m^{-2} sec^{-1}, and then OERs were assayed across a range of light intensities. The lower OER in *sta6* (Figure 2a) indicates that either PSII itself is impaired and/or that reactions downstream of PSII are affected at light intensities >60 μE m^{-2} sec^{-1}. To differentiate between the two processes, we assessed the light-induced electron transport rate (ETR) through PSII and the quantum yield of PSII charge separation and the turnover efficiency of the water-oxidizing complex (WOC). The light-induced ETR through PSII was measured using a pulse-amplitude modulated fluorometer (Schreiber *et al.*, 1997) (Figure 2b). This method indicates the proportion of open PSII centers capable of photoreducing Q_A as a function of the light intensity of concurrent background illumination. Although widely used to measure ETR (flux), this signal is

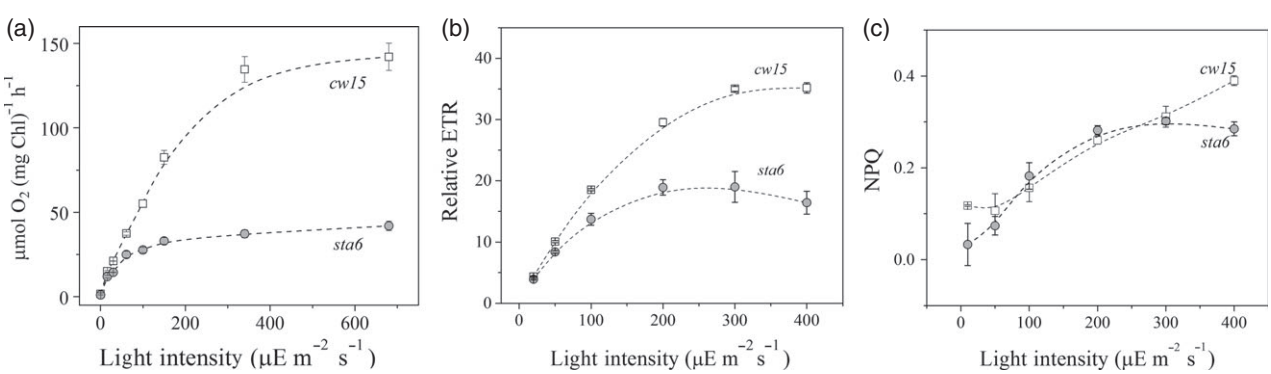

Figure 2. Oxygen evolution rate, ETR and NPQ. (a) Oxygen evolution rates at various actinic light intensities (16, 30, 61, 100, 150, 340 and 680 μE m^{-2} sec^{-1}) measured (at mid-log phase growth, Figure 1).
(b) Relative electron transport rate (ETR).
(c) NPQ measured by a pulse-amplitude modulated fluorometer.
Values are means and standard errors of three biological replicates.

a static measure of the Q_A population. It is proportional to the sum of ETR flux and photochemical quenching that does not lead to electron transfer beyond PSII. For this reason, the pulse-amplitude modulated measurement of ETR includes non-flux contributions to photochemical quenching within PSII that produce no O_2. The ETR curves show a trend that is qualitatively similar to that for OER, with *sta6* and *cw15* showing no significant differences at the lowest light intensities, but with differences between *sta6* and *cw15* emerging at approximately 75 μE m^{-2} sec^{-1}. *sta6* shows substantially lower ETRs at light intensities above 200 μE m^{-2} sec^{-1}. At the maximum light intensity used for the measurement (approximately 400 μE m^{-2} sec^{-1}), the ETR in *sta6* was approximately twofold lower than that in *cw15*. The ETR in *sta6* is also saturated at a lower light intensity (200 μE m^{-2} sec^{-1}). The percentage differences observed in OER are larger than the differences in ETR (Figure S1) at all light intensities, and the difference becomes larger as the intensity increases. This comparison shows that light-induced O_2 consumption reactions contribute to ETR more significantly in *sta6* than *cw15*. To investigate the possibility of non-photochemical quenching (NPQ)-dependent decreases in ETR, NPQ was quantified simultaneously with ETR using the method described by Schreiber *et al.* (1997), and calculated as described in Experimental procedures. *sta6* and *cw15* do not show significant differences in NPQ (Figure 2c), and thus the differences in ETR are not due to differences in excitation quenching in the antenna.

To examine whether an impaired PSII WOC activity is the cause of the low OER and ETR phenotype, the quantum yield of PSII charge separation and flux through the WOC were measured as chlorophyll variable fluorescence emission (F_v/F_m) using a fast repetition rate fluorometer at two flash frequencies (Ananyev and Dismukes, 2005). Compared to *cw15*, *sta6* exhibits a slightly lower steady-state dark-adapted F_v/F_m under both a low flash frequency (4 Hz, $<F_v/F_m>$ approximately 0.43–0.41) and a high flash frequency (100 Hz, $<F_v/F_m>$ approximately 0.24–0.18) (Figure 3a). Following an initial dark adaptation, the rate of damping of the period four oscillations in F_v/F_m was similar for both strains, and decreased at higher flash rates (Figure 3a), indicating that both strains have normal initial WOC activity. Fitting of the oscillations to an advanced Kok model (VZAD algorithm) (Vinyard *et al.*, 2013) produce almost identical hit parameters (γ_{avg}) and periods (P) at both flash frequencies, indicating no significant difference in the initial turnover probability of the WOC in the two strains. However, the initial rate of damping of individual oscillations in F_v/F_m decreases rapidly with a higher flash rate (γ_{avg} decreases to 0.57 at 100 Hz, Figure 3a), and the non-oscillating portion of F_v/F_m in *sta6* lacks the portion attributed to filling of the PQ pool (hatched area in Figure 3a) (Kolling *et al.*, 2009). Thus, *sta6* is characterized by

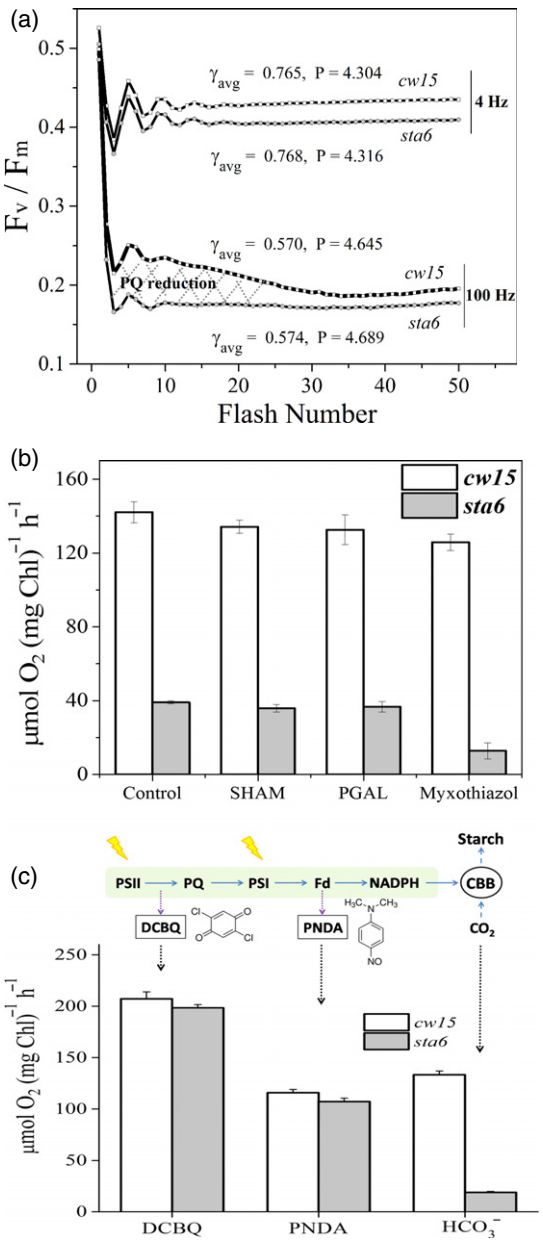

Figure 3. Variable fluorescence, metabolic inhibitors and electron transport chain acceptors. (a) Mean chlorophyll variable fluorescence yield (F_v/F_m) from PSII produced by 50 single-turnover laser flashes at two flash rates (4 and 100 Hz). The mean Kok hit parameter, γ_{avg}, was determined by fitting the data to the VZAD model: $\gamma_{avg} = 1 - \alpha$ (miss) $- \beta$ (double hit) $- \delta$ (backward) $- \varepsilon$ (inactivated). The cycle period, P, was determined by Fourier transformation. The shaded region represents the reduced PQ pool.
(b) OER of *cw15* and *sta6* in the presence of inhibitors to the alternative electron flow pathway at 680 μE m^{-2} sec^{-1}. The control contains 5 mM bicarbonate, salicylhydroxamic acid (SHAM, 20 μM) inhibits alternative oxidase, propyl gallate (PGAL, 2 mM) inhibits plastoquinol terminal oxidase, and myxothiazol (2 μM) inhibits respiration.
(c) Light-saturated OERs (680 μE m^{-2} sec^{-1}) in the presence of artificial electron acceptors (40 μM 2,5–dichloro-*p*–benzoquinone, 400 μM *N*–dimethyl-4–nitrosoaniline or 5 mM $NaHCO_3$). Values are means and standard errors of three biological replicates.

a slower rate of emptying of the reduced plastoquinol PQH_2 pool relative to *cw15*.

Thus, both strains have a normal functioning WOC and PSII charge separation, but *sta6* has an inhibited PQH_2 oxidation rate, reflecting a blockage in electron flow downstream of the PQH_2 pool. This blockage is responsible for the sharp break in OER flux at a light intensity >100 μE m^{-2} sec^{-1} (Figure 2a).

Alternative oxygen-consuming pathways

As previously mentioned, at higher light intensities, there is an imbalance in the extent of inhibition indicated by OER versus ETR, with OER predicting a lower intensity threshold and larger activity gap at saturation between *sta6* and *cw15* (Figure S1). This difference indicates the presence of alternative O_2-consuming pathways that influence OER and ETR differently at light intensities above 100 μE m^{-2} sec^{-1}. The main pathways that consume O_2 are respiration and alternative oxidases in the mitochondrion, as well as plastoquinol terminal oxidase, the Mehler reaction and photorespiration in the chloroplast. Inhibition of alternative oxidases and plastoquinol terminal oxidase (also known as chlororespiration) by the specific inhibitors salicylhydroxamic acid (20 μM) and propyl gallate (2 mM), respectively, did not have any significant effect on the OER (at 680 μE m^{-2} sec^{-1}) in either *cw15* or *sta6* (Figure 3b). However, inhibition of mitochondrial respiration by myxothiazol (inhibiting the cytochrome bc_1 complex of the respiratory chain) leads to a 70% reduction of the OER in *sta6*, but only a minor reduction (10%) in *cw15* (Figure 3b) (at 680 μE m^{-2} sec^{-1}). Thus, only in *sta6* does mitochondrial respiration act as an important shunt to partially consume the excess light-induced reductant generated in the chloroplast. Further measurements of the Mehler reaction and photorespiration were not performed, although Figure S1 clearly indicates their possible contributions to reductant re-oxidation.

Normal PET rates through PSII and PSI may be restored in *sta6*

The above results suggest that, under high light intensities, photosynthesis in *sta6* is limited by the reactions occurring downstream of PSII, either within the electron transport chain itself (light-dependent reactions) or by carbon fixation reactions (light-independent reactions). To distinguish between these options, artificial electron acceptors were used to alleviate bottlenecks in the PET chain, and the corresponding OER was measured at 680 μE m^{-2} sec^{-1}. As shown in Figure 2(c), in the presence of 2,5–dichloro-*p*–benzoquinone (40 μM), which accepts electrons from the Q_B site of PSII, the OER of both *sta6* and *cw15* increased to approximately 200 μmol O_2 mg chlorophyll^{-1} h^{-1}. In the presence of *N*–dimethyl-4–nitrosoaniline (400 μM), which accepts electrons from photosystem I (PSI) via ferredoxin, both strains had an equal OER of approximately 110 μmol O_2 mg chlorophyll^{-1} h^{-1}. These experiments show that *sta6* has a structurally intact electron transport chain similar to that of *cw15* through ferredoxin, with normal fluxes and similar electron acceptor pool sizes (for PQ and ferredoxin). Bicarbonate addition to ensure saturating levels for carbon fixation reactions (Figure 3b) did not reverse the disparity in OER between *cw15* and *sta6*. Thus, the OER in *sta6* is limited downstream of ferredoxin by carbon fixation reactions.

To further isolate the location of flux bottlenecks, we measured the light-induced yield of O_2 from a thin solution layer of cells (0.8 mm) illuminated at 400 μE m^{-2} sec^{-1} using a bare platinum (rate) electrode. This method resolves kinetic features of the electron acceptor pools downstream of PSII (Zakrzhevskii *et al.*, 1978). A typical O_2 evolution trace after dark adaptation displays three distinct time-resolved features. The first is a sharp transient peak from reduction of the PQ pool, the second is a broad peak arising from reduction of $NADP^+$, and the third is a continuous slope arising from CO_2-dependent O_2 evolution. The initial peak has a rise time of 300 msec due to O_2 diffusion to the electrode, and is determined by the finite thickness of the sample. The area under this peak (see Experimental procedures) is directly proportional to the difference in electron fluxes filling and emptying the oxidized PQ pool. The PQ peak intensity and area are indistinguishable for *sta6* and *cw15*. In *cw15*, a second O_2 feature appears as an inflection (Figure 4, top), but this is masked by a much larger continuous slope that disappears when CO_2 is removed (data not shown) or when the PET inhibitor 3–(3,4–dichlorophenyl)-1,1–dimethylurea is added (Figure 4, bottom). This CO_2-dependent water oxidation rate is sevenfold greater in *cw15* than in *sta6* over the illumination period shown (400 μE m^{-2} sec^{-1}).

To quantify the transient flux into and out of the NADP (H) pool, the relative light-induced yield of the reaction PSI donor → $NADP^+$ was monitored by the fluorescence change from reduced NAD(P)H *in vivo*. NAD(P)H kinetics in whole cells were measured using a home-built fluorometer (excitation at 365 nm, detection at 420 nm) similar to that described by Mi *et al.* (2000). Samples were exposed to a dark/light/dark regime of 5 min/4 min/7 min using saturating light (400 μE m^{-2} sec^{-1}, 660 nm). Curves derived from three biological replicates for *sta6* and two for *cw15* are shown in Figure 5(a), with results for individual replicates shown in Figure S2A. The rise and decay times and the amplitude changes of the fluorescence yield are given in Table 2. Light-induced changes in NAD(P)H fluorescence display dynamics similar to those described in previous reports (Cerovic *et al.*, 1993; Mi *et al.*, 2000). We observed an increase in NADPH fluorescence emission during actinic illumination, signifying light-driven reduction of $NADP^+$, followed by a steady-state phase during which the $NADP^+$

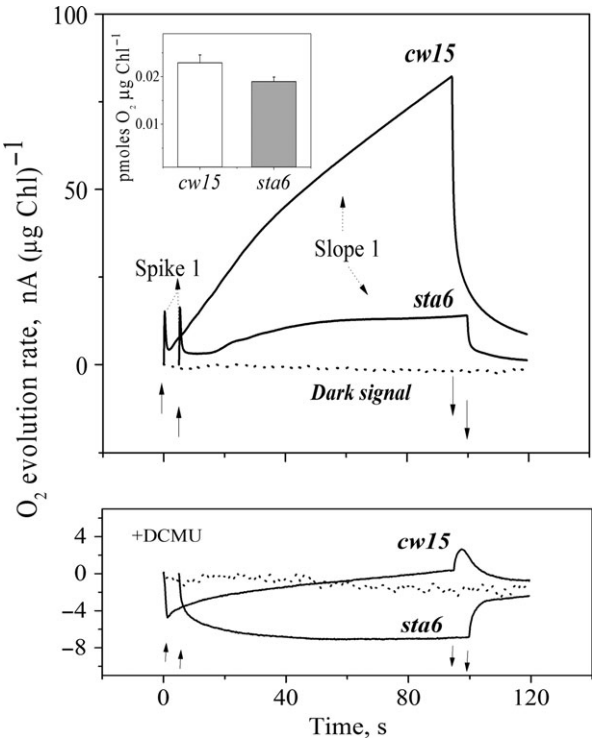

Figure 4. Light-saturated OERs (400 μE m^{-2} sec^{-1}) on a bare platinum electrode recorded as nanoAmperes (μg chlorophyll)$^{-1}$ in the presence of bicarbonate as the sole electron acceptor.
Values are means of three biological replicates. Light was turned on or off at the points indicated by solid arrows. Transient O_2 evolution shows two distinct phases: spike 1 represents the PQ pool reduction, while the continuous slope represents carbon fixation (top panel). The inset shows the PQ pool size equivalent calculated as described in Experimental procedures. The bottom panel shows the effect of 10 μM 3–(3,4–dichlorophenyl)-1,1–dimethylurea (DCMU) on the OER. The dotted line represents the current recorded in the absence of illumination.

reduction and NAD(P)H oxidation rates are matched. After illumination (i.e. in darkness), the fluorescence decays, followed by recovery to the initial steady-state dark level. In the presence of the artificial PSI electron acceptor *N*–dimethyl-4–nitrosoaniline, both *sta6* and *cw15* show no change in NAD(P)H fluorescence upon illumination (Figure S2B).

The NAD(P)H fluorescence yield increases from the dark-adapted level to the maximal photoreduced level over identical time periods for both strains (t_1 = 7.2 sec). During the illumination period, the larger photoinduced amplitude in *sta6* decreases slowly to 50% with a lifetime of approximately 2.9 min (t_2), but the lower photoinduced amplitude for *cw15* does not decay appreciably over the measurement time scale. The larger amplitude and gradual decaying slope of light-induced NADPH in *sta6* are attributed to slower NADPH re-oxidation. This was verified by turning off the actinic light and monitoring the decay rate of the NADPH fluorescence amplitude (Y_2), which is indeed slower in *sta6* (t_3 = 20 sec) than *cw15* (t_3 = 14 sec), and 'overshoots' to a level lower than the initial steady-state dark level. The t_3 decay rate in *cw15* is followed by recovery to the initial steady-state level within 39 sec (t_4), as the non-equilibrium level of oxidized $NADP^+$ is re-reduced in the dark. Such oscillating behavior is commonly associated with regenerative cycles. This latter phase is absent in *sta6*. Taken together, the lack of overshoot, slower t_3 decay, and slow decay of the actinic phase (t_2) all support the conclusion of a slower re-oxidation rate of actinically generated NADPH in *sta6*. For *cw15*, the lack of observable decay of the actinically generated NADPH phase indicates a rate of NADPH re-oxidation faster than the time resolution of the instrument (approximately 1 sec).

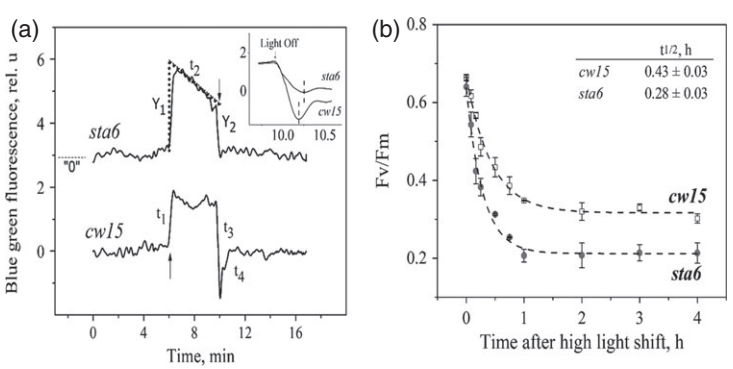

Figure 5. NADP(H) reoxidation and photoinhibition. (a) Effect of actinic illumination on induction of a continuous level of blue/green fluorescence arising from NAD(P)H. Actinic illumination was provided by saturating red light (660 nm, intensity = 400 μE m^{-2} sec^{-1}). Light was turned on or off at the points indicated by solid arrows. The fluorescence decay during illumination (lifetime indicated by t_2 for *sta6*) was fitted to a linear decay slope and extrapolated to 'light on' time to calculate the maximal photoreduced NADPH (Y1) in the absence of oxidation of NADPH. Y2 denotes the oxidized NADPH post-illumination. t_1, t_2, t_3 and t_4 are the rise and decay times as described in the text. A magnification of the decay kinetics is shown in the inset. The results for sta6 are offset by 3 units in (a).
(b) Photoinhibition at 400 μE m^{-2} sec^{-1}, the $t_{½}$ values for photoinhibition are given in the inset table. Values are means and standard errors of three biological replicates.

Table 2 Kinetics of $NADP^+$ reduction and NADPH re-oxidation

Parameters	*cw15*	*sta6*	Fold change (*sta6*/*cw15*)
Rise time, t_1 (sec)	7.2 ± 0.3	7.2 ± 0.42	1.0 ± 0.07
Re-oxidation time, t_2 (min)	≤ t_1	2.9 ± 0.67	
Decay time, t_3 (sec)	14 ± 0.6	20 ± 2.4	1.4 ± 0.12
Re-reduction rate, t_4 (sec)	39 ± 0.6	–	
Maximum photoreduced NADPH, Y_1 (relative units)	1.5 ± 0.04	2.6 ± 0.3	1.7 ± 0.12
Oxidized NADPH post-illumination, Y_2 (relative units)	2.8 ± 0.3	1.9 ± 0.2	0.68 ± 0.15

Values are means ± SEM for three biological replicates.

sta6 is more sensitive to photoinhibition

Sensitivity to photoinhibition upon prolonged high-light exposure was determined by measuring the loss of PSII quantum yield (as F_v/F_m) in samples incubated under light (400 μE m^{-2} sec^{-1}, 620 nm) over a period of 6 h (Figure 5b). *sta6* exhibits a 35% faster photoinhibition rate than in *cw15* (half life = 0.28 h versus 0.43 h), indicating the importance of starch biosynthesis for tolerance to high-light stress.

sta6 is inefficient in drain upper glycolytic intermediates at high light intensity

Given that OER and ETR are significantly inhibited at high light intensities and the metabolic block occurs downstream of PET, comparative metabolic analysis of samples treated under low light (LL) or high light (HL) was performed to reveal the metabolic consequences of the decrease in NADPH re-oxidation. The pool sizes of various metabolites involved in central carbon metabolism were measured using LC-MS/MS (Bennette *et al.*, 2011) under ambient growing conditions (approximately 60–80 μE m^{-2} sec^{-1}, low light) and after a 2 h exposure to high light (400 μE m^{-2} sec^{-1}). Concentrations of the metabolites are shown in Table 3. The results for metabolites of the Calvin–Benson–Bassham (CBB) cycle and upper glycolysis are summarized in Figure 6(a,b). Simultaneously, the biomass contents (lipids, TRC and protein) were also measured (Figure 6c) using the same cultures.

Upon transfer to HL, neither protein nor lipids showed a significant change in the two strains. However, the TRC content per cell increased by 25% in *cw15* but was unchanged in *sta6* (Figure 6c). Thus, under 2 h exposure to HL, fixed carbon predominantly accumulates as starch, whereas blocking starch biosynthesis at AGPase in *sta6* impedes carbon assimilation into all biopolymers.

Metabolite analysis revealed that, under HL, *cw15* shows an increase in CBB cycle intermediates including ribulose-1,5–bisphosphate (fivefold), ribose-5–phosphate (fourfold) and xylose-5–phosphate (ninefold) compared to LL. Glyceraldehyde phosphate and 3–phosphoglycerate levels also increase by approximately twofold (Figure 5a and Table 3). This increase correlates with the enhanced carbon assimilation in *cw15* (Figure 6c). Even though the TRC content increases in *cw15* (Figure 6c), there is no increase in the pool size of upper glycolytic intermediates, indicating an efficient drain of the upper glycolytic metabolites into carbohydrate biosynthesis. By contrast, in *sta6*, we observed large increases in the levels of many CBB cycle metabolites, especially the glyceraldehyde phosphate and 3–phosphoglycerate levels, which increased by eleven- and sevenfold, respectively. Additionally, we observed increased levels of the upper glycolytic intermediates glucose-1–phosphate, glucose-6–phosphate and fructose-6–phosphate (fivefold, fourfold and eightfold, respectively), even though there is no significant increase in the TRC content. Thus, under HL conditions and in the absence of AGPase, there is an inefficient drain of the upper glycolytic intermediates that normally flow into starch biosynthesis.

A lower ATP recycling rate may limit electron transport chain flux (Sharkey *et al.*, 1986). To test this, the adenine nucleotide concentrations were quantified using LC–MS, and the cellular energy charge was calculated (Table 3). *sta6* shows appreciably higher concentrations of all adenine nucleotides (ATP, ADP and AMP) in *sta6* relative to *cw15* under both LL and HL. Additionally, *sta6* has a marginally larger pool size of the phosphorylated pyridine nucleotides relative to *cw15* (Table 3). This increase in both NADP(H) and adenylates probably reflects the cellular response to *sta6*'s inability to use the CBB intermediates in starch biosynthesis. Although the cellular energy charge did not differ in the two strains under either light regime, the method we used may not be rapid enough to prevent equilibration. A stable cellular energy charge is known to be essential for normal cellular function (Kramer and Evans, 2011).

Photosynthetically fixed carbon in *sta6* is re-directed towards the lower glycolytic pathway

Metabolites of the central carbon metabolism outside the CBB cycle and involved in biosynthesis of amino acids, fatty acids and alternative CO_2 fixation (C4) were quantified and compared across the two strains (Table 3). In *sta6*, levels of the high-energy phosphate ester phosphoenolpyruvate increasedfourfold, further indicating accumulation of excess cellular phosphate and energy. Among the tricarboxylic acid cycle metabolites, succinate and α–ketoglutarate increased uniformly in both strains. Although *sta6* does not accumulate protein, the amino acid precursors glutamine and glutamate increased under both LL and HL compared to *cw15*. Significantly, from the perspective of lipid biosynthesis, the level of the fatty acid precursor

Table 3 LC-MS/MS results for various metabolites

Metabolite	Abbreviation	*cw15* under LL[a]	*cw15* under HL[b]	*sta6* under LL[a]	*sta6* under HL[b]	Fold change for *cw15* (HL/LL)[c]	Fold change for *sta6* (HL/LL)[c]	*P* value for *cw15*	*P* value for *sta6*
Glycolysis and CBB intermediates									
ADP-glucose	ADP-glc	0.019 (0.003)	0.010 (0.001)	0.001 (0.001)	0.001 (0.000)	0.515 (0.102)	0.675 (0.311)	*0.043*	*0.470*
Glucose-1–phosphate	G1P	0.115 (0.006)	0.086 (0.017)	0.063 (0.004)	0.357 (0.091)	0.745 (0.152)	**5.63** (1.19)	*0.179*	*0.022*
Glucose-6–phosphate	G6P	0.101 (0.001)	0.076 (0.025)	0.064 (0.004)	0.291 (0.104)	0.753 (0.246)	**4.53** (1.14)	*0.373*	*0.046*
Fructose-6–phosphate	F6P	0.058 (0.006)	0.055 (0.029)	0.038 (0.001)	0.313 (0.118)	0.950 (0.509)	**8.27** (1.63)	*0.927*	*0.050*
Glyceraldehyde phosphate	GAP	0.077 (0.002)	0.195 (0.048)	0.040 (0.002)	0.474 (0.183)	**2.51** (0.626)	**11.8** (2.58)	*0.059*	*0.041*
3–Phosphoglycerate	3PG	3.00 (0.091)	5.69 (0.812)	0.386 (0.058)	2.87 (1.091)	**1.89** (0.277)	**7.45** (1.04)	*0.030*	*0.035*
Phosphoenolpyruvate	PEP	0.736 (0.041)	1.27 (0.210)	0.160 (0.014)	0.702 (0.264)	**1.72** (0.302)	**4.38** (1.695)	*0.067*	*0.110*
Acetyl CoA	AcCoA	0.116 (0.003)	0.231 (0.030)	0.205 (0.014)	0.119 (0.042)	**1.99** (0.263)	0.581 (0.209)	*0.018*	*0.125*
Ribulose-1,5–bisphosphate	RuBP	0.082 (0.011)	0.337 (0.019)	0.019 (0.002)	0.099 (0.037)	**4.10** (0.583)	**5.10** (0.906)	*0.000*	*0.038*
Ribose-5–phosphate	R5P	0.012 (0.002)	0.039 (0.006)	0.013 (0.002)	0.046 (0.016)	**3.18** (0.680)	**3.62** (1.37)	*0.015*	*0.108*
Xylose-5–phosphate	X5P	0.015 (0.003)	0.071 (0.026)	0.010 (0.002)	0.091 (0.031)	**4.77** (2.08)	**9.34** (3.76)	*0.105*	*0.059*
Sedoheptulose-7–phosphate	S7P	0.074 (0.022)	0.575 (0.145)	0.061 (0.017)	0.507 (0.174)	**8.21** (3.6)	**7.74** (3.01)	*0.063*	*0.027*
Lipid precursor									
Malonyl CoA	MaCoA	0.001 (0.000)	0.001 (0.000)	0.018 (0.000)	0.028 (0.002)	0.968 (0.296)	1.59 (0.071)	*0.9195*	*0.026*
Tricarboxylic acid cycle and amino acids									
Succinate	SUCC	0.712 (0.058)	1.49 (0.131)	0.304 (0.044)	0.594 (0.164)	**2.09** (0.251)	**1.95** (0.608)	*0.006*	*0.161*
Malate	MAL	1.86 (0.108)	2.63 (0.201)	1.17 (0.152)	1.67 (0.456)	1.41 (0.136)	1.42 (0.429)	*0.028*	*0.360*
α–ketoglutarate	AKG	0.452 (0.017)	1.13 (0.334)	0.169 (0.030)	0.343 (0.096)	**2.50** (0.746)	**2.03** (0.675)	*0.112*	*0.159*
Glutamate	GLU	3.32 (0.177)	5.80 (0.378)	2.28 (0.106)	5.35 (1.29)	1.44 (0.147)	**2.34** (0.578)	*0.004*	*0.077*
Glutamine	GLN	0.046 (0.002)	0.062 (0.001)	0.082 (0.019)	0.057 (0.018)	1.34 (0.071)	**2.08** (0.276)	*0.003*	*0.056*
Sugars									
Sucrose	SUCR	0.011 (0.004)	0.014 (0.002)	0.007 (0.001)	0.044 (0.017)	1.20 (0.421)	**6.10** (2.488)	*0.598*	*0.062*
Energy carriers									
AMP	AMP	1.66 (0.171)	1.60 (0.830)	2.09 (0.521)	2.67 (1.19)	**2.16** (0.656)	**2.71** (1.329)	*0.137*	*0.217*
ADP	ADP	2.20 (0.206)	2.84 (0.363)	3.43 (0.396)	3.98 (2.23)	1.28 (0.231)	1.15 (0.572)	*0.549*	*0.717*
ATP	ATP	3.40 (0.183)	3.92 (0.826)	6.48 (1.35)	6.21 (1.21)	1.15 (0.256)	0.958 (0.285)	*0.923*	*0.727*
Cellular energy charge									
$\frac{ATP+(0.5*ADP)}{ATP+ADP+AMP}$	CEC	0.682 (0.060)	0.637 (0.023)	0.620 (0.022)	0.638 (0.076)				
Pyridine nucleotides									
NAD^+ + NADH		1.92 (0.043)	3.06 (0.286)	2.74 (0.118)	2.348 (0.670)	1.43 (0.048)	0.767 (0.300)	*0.454*	*0.752*
$NADP^+$ + NADPH		0.636 (0.052)	0.873 (0.073)	0.781 (0.027)	1.13 (0.262)	1.22 (0.088)	1.29 (0.246)	*0.213*	*0.783*

Values are means. Standard errors of the mean are given in parentheses.
Bold numbers denote the metabolites with a 1.5-fold higher or 1.5-fold lower metabolic concentration under HL w.r.t LL. *P*-values are italicized.
[a,b]Concentration of the the metabolites in *sta6* and *cw15* under low-light conditions (steady state) or high-light conditions, calculated as μmol per 10^8 cells.
[c]Fold change in concentration of the metabolites between LL and HL in *sta6* and *cw15*, calculated as [HL]/[LL].

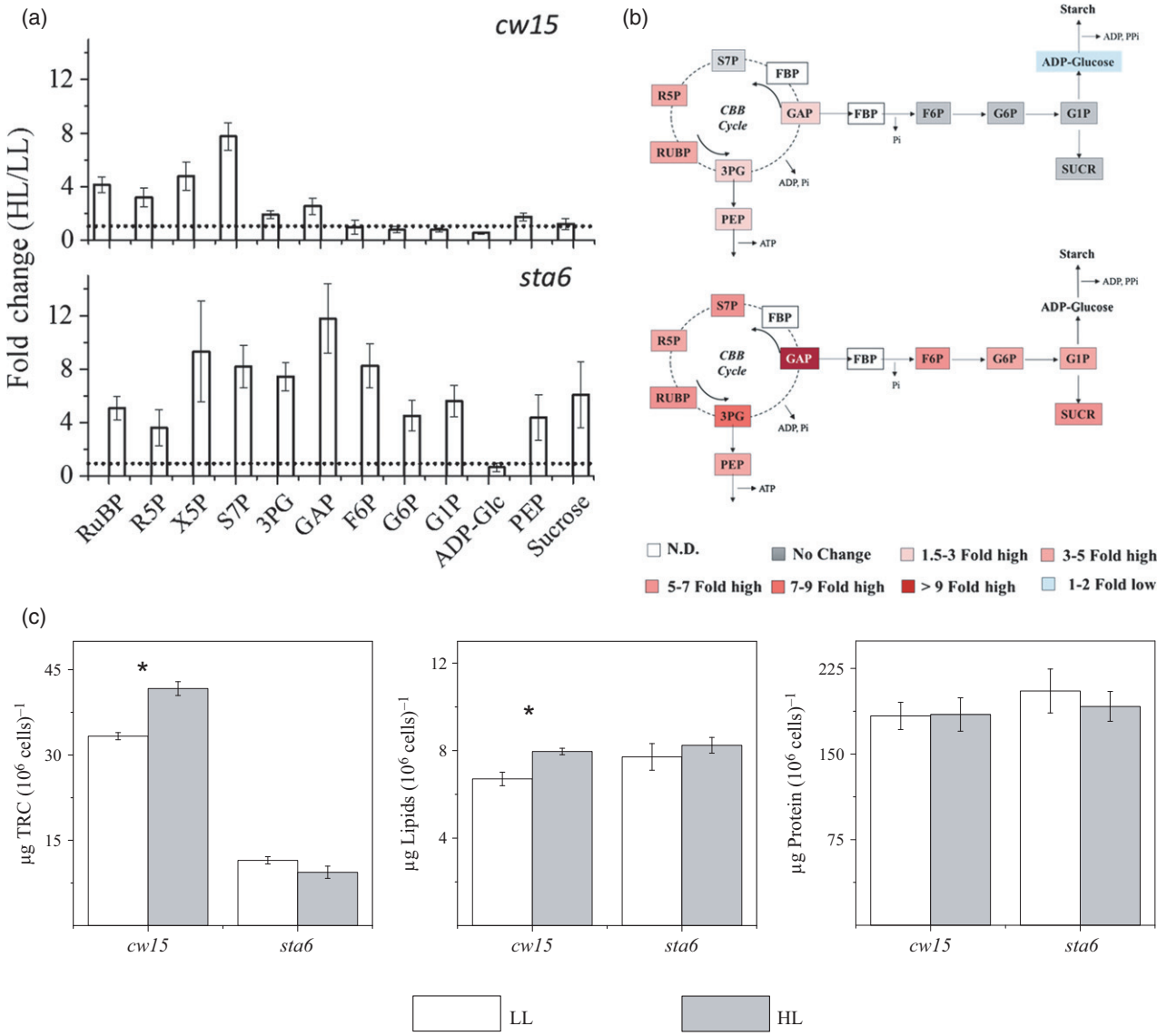

Figure 6. Metabolite and biomass distribution.
Summary of metabolomics data for the CBB cycle and gluconeogenic pathway.
(a) Fold changes in the metabolites occurring during LL to HL transition in *sta6* and *cw15*. The dotted line represents no change.
(b) Schematic representation of the fold changes for the metabolites shown in (a).
(c) Biomass distribution (TRC, lipids and proteins) during the LL to HL transition.
Values are means and standard errors of three biological replicates. The asterisk indicates a statistically significant difference compared with *cw15* ($P < 0.05$).

malonyl CoA is 18-fold higher in *sta6* compared to *cw15*, and increased further to 28-fold under HL, although the total lipid content in *sta6* was indistinguishable from that in *cw15*.

DISCUSSION

Various starchless mutants have been used as test strains in search of higher lipid producers in many previous studies (Wang *et al.*, 2009; Li *et al.*, 2010a,b; Work *et al.*, 2010; Goodson *et al.*, 2011; Siaut *et al.*, 2011; Fan *et al.*, 2012; Blaby *et al.*, 2013; Goodenough *et al.*, 2014). These studies also found that loss of starch synthesis and lower growth rates were strongly correlated, but the consequences on the individual PET reactions and carbon partitioning via pathways and into terminal products had not been examined systematically at the molecular level. Scheme 1 summarizes our data describing the molecular phenotypes arising from loss of AGPase in the *Chlamydomonas* starchless mutant *sta6*.

Starch biosynthesis (or glycogen biosynthesis in cyanobacteria) is essential for (at least) four reasons: (i) consuming the photosynthetically generated reductant

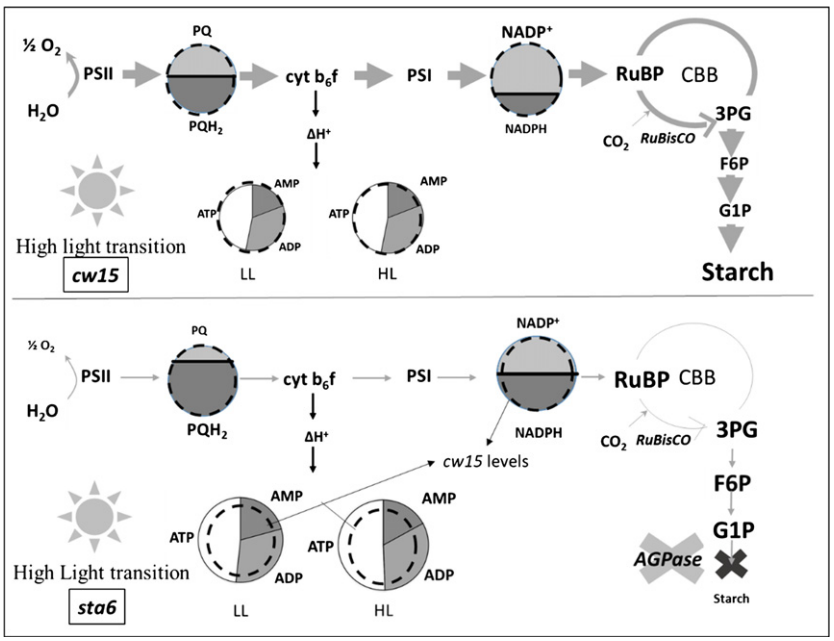

Scheme 1. Schematic representation of light-dependent and -independent reactions of photosynthesis in the *sta6* strain (deletion in the small subunit of AGPase, indicated by the cross); *cw15* is the control strain. Thick and thin arrows represent large and small electron fluxes through WOC, PET and the CBB cycle, with *sta6* having a twofold slower electron flux than *cw15*. Small and large font sizes indicate (qualitative) differences in relative contents. Circle areas are proportional to the total pool sizes in the cell (dashed circle for *cw15*, solid circles for *sta6*). The dashed circles in the *sta6* panel show the pool size of the metabolite in *cw15* superimposed onto the *sta6* pool size, indicating that *sta6* has a larger pool size of NADP(H) (1.2-fold) and adenylates (1.6-fold) versus *cw15*, but similar plastoquinone pool sizes. The ratio of NADPH/NADP$^+$ and plastoquinol/plastoquinone pool sizes is qualitatively indicated using dark and light gray.

(NADPH) and ATP (Kramer and Evans, 2011), (ii) providing a gluconeogenic route for replenishing CBB cycle intermediates, (iii) to produce a storage product with low osmotic potential to meet carbon and energy needs in the dark, and (iv) for photoprotection against oxidative damage. In the absence of starch biosynthesis arising from a non-functional AGPase, all of these functions are disrupted. Especially under high light, the primary effect is on the rate of CO_2-dependent water oxidation, with *sta6* having a 3.5-fold slower rate than *cw15* (Figure 2a). This leads to a build-up in the reductant poise (NADPH/NADP$^+$), the extent of carbohydrate phosphorylation, and the level of adenylate nucleotides, the latter presumably in an attempt to compensate for the slower turnover rate (Scheme 1). Accumulation of several phosphorylated carbohydrates (Table 3 and Scheme 1) and the upper glycolysis intermediates glucose-1–phosphate, glucose-6–phosphate and fructose-6–phosphate occurs, and these do not drain efficiently to terminal sinks. This outcome, together with the 2.8-fold larger adenylate pool size, results in a corresponding decrease in the free inorganic phosphate (Pi) in the stroma of the chloroplast. In addition, the increased ATP would complex with Mg^{2+} (Storer and Cornish-Bowden, 1976) leading to a decrease in the free Mg^{2+} as well. As Mg^{2+} and free Pi are required activators for RuBisCO and other CBB enzymes, allosteric down-regulation of RuBisCO dependent CO_2 fixation activity is expected in sta6. This down-regulation appears to be directly responsible for the slowing of NADPH oxidation, and the ultimately slowing of all PET reactions as far upstream as water oxidation by PSII. The CBB cycle appears to be the main target affected by the AGPase mutation in *sta6*, as none of the individual PET enzyme fluxes exhibit inhibition relative to the *cw15* control when measured in isolation. Our results with PET electron acceptors (Figure 3c) confirm that, like typical wild algal strains (Rochaix, 2011), re-oxidation of the PQ pool is retained in *sta6* as the slowest kinetic step of the PET chain. *sta6* uses mitochondrial respiration to help relieve aspects of cellular over-reduction (Figure 3b). By contrast, inhibition of mitochondrial respiration in *cw15* leads to a comparatively insignificant effect on the OER. Thus, respiration appears to be critical for sustaining the low level of photosynthetic oxygen evolution in *sta6*. Consistent with this observation, P700$^+$ kinetics are impaired when respiration is inhibited in *sta6* (Johnson and Alric, 2012). For conditions under which *sta6* is unable to maintain redox homeostasis, it does not depend on plastoquinol terminal oxidase or alternative oxidases but potentially uses the Mehler reaction or photorespiration to reduce O_2 and remove the excess reductant. Thus alternative O_2-consuming pathways become important for supporting light-induced ETR as redox valves in *sta6.*

The large fourfold increase in phosphoenolpyruvate concentration in *sta6* is interesting as this molecule is known to function in another CO_2 fixation pathway via phosphoenolpyruvate carboxylase, which may therefore become more important in *sta6*. Phosphoenolpyruvate carboxylase catalyzes the reaction that combines bicarbonate (HCO_3^-) and phosphoenolpyruvate to form oxaloacetate. This is an anaplerotic reaction that is important for synthesis of amino acids (Ala, Asp, Glu). Phosphoenolpyruvate carboxylase-dependent carbon fixation may even exceed the amount of carbon fixed via the CBB cycle in some unicellular algae under nitrogen-limited conditions (Guy *et al.*, 1989).

sta6 has smaller hexose phosphate pool sizes under low light, which may reflect the attenuation of photosynthesis, decreased carbon fixation, and/or re-direction of fixed carbon to the tricarboxylic acid cycle for protein synthesis. Under HL conditions, when increased levels of photosynthate enter the central metabolism, the tricarboxylic acid cycle appears to become saturated (Table 3), resulting in accumulation of hexose phosphate metabolites. Determination of the precise underpinnings of these phenotypes requires additional experimentation, and metabolic flux analysis is required to obtain a more informed understanding of the observed dynamic re-direction of metabolites.

Even though over-reduction of the PET chain is relieved in part by mitochondrial respiration in *sta6* (Figure 3b), prolonged exposure to high light leads to accelerated photoinhibition relative to *cw15* (Figure 5b), indicating that starch production is an important safeguard against photodamage. The light-driven accumulation of excess NADPH and reduced ferredoxin lead to formation of reactive oxygen species in many aquatic phototrophs and plants. A similar phenotype was observed in several other characterized AGPase mutants (Sun *et al.*, 1999; Suzuki *et al.*, 2010; Grundel *et al.*, 2012). As starch is the least energy-intensive terminal product among starch, proteins and lipids, it may serve as an energy storage buffer to protect against light energy fluctuations and to enable biosynthesis of these more energy-intensive biopolymers during low light periods, similar to that postulated in higher plants (Caspar *et al.*, 1985; Stitt and Quick, 1989; Ludewig *et al.*, 1998; Geigenberger, 2011; Weise *et al.*, 2011).

Carbon that enters the central metabolism from the CBB cycle may take two possible routes: the upper gluconeogenesis pathway leading into C6 and C5 carbohydrates, or the lower glycolytic pathway leading to acetyl CoA that either enters the tricarboxylic acid cycle to synthesize amino acids or is converted to malonyl CoA to synthesize lipids. Several groups have reported increased lipid yields in *sta6* after switching cells to a nitrogen-deficient growth medium (Wang *et al.*, 2009; Li *et al.*, 2010a,b; Work *et al.*, 2010; Goodson *et al.*, 2011; Siaut *et al.*, 2011; Fan *et al.*, 2012). Increased lipid accumulation is not observed under nutrient-replete, photoautotrophic conditions in *sta6*; instead growth is stunted. However, there is a major increase in both acetyl CoA and malonyl CoA levels in *sta6*. Malonyl CoA formation is catalyzed by acetyl CoA carboxylase (ACCase) through an ATP-dependent carboxylation of biotin that transfers a carboxyl group to acetyl CoA (Berg *et al.*, 2002). The ACCase reaction is considered to be the committed step in fatty acid synthesis. It is regulated by reversible phosphorylation catalyzed by an AMP-dependent protein kinase (Berg *et al.*, 2002). ACCase is inhibited by phosphorylation, while the unphosphorylated form has carboxylase activity. AMP-dependent protein kinase itself acts as an adenylate nucleotide sensor, being activated by high AMP levels and inhibited by high ATP levels (Berg *et al.*, 2002; Hardie and Pan, 2002). As such, the kinase activity becomes self-limiting at high ATP concentrations. Accumulation of malonyl CoA in *sta6* indicates a reversal of inhibition of ACCase relative to *cw15*. Given that ATP accumulates in *sta6* (Table 3), we predict that the higher ATP content probably inhibits AMP-dependent protein kinase, and, in turn, enhances the carboxylase activity of ACCase. Thus, simple over-expression of ACCase may not be enough to enhance ACCase activity, but instead needs to occur in parallel with reducing the level of phosphorylation of ACCase, which is achieved by suppression of AMP-dependent protein kinase phosphorylation activity. Taken together, the higher ATP accumulation in *sta6* cells metabolically poises it for higher levels of fatty acyl biosynthesis, as indicated by elevated levels of acetyl CoA and especially malonyl CoA, but downstream blockage in the fatty acid synthesis complex putatively prevents utilization. Our data show that factors beyond availability of the precursor (malonyl CoA) control the flux into lipid biosynthesis. Under photoautotrophic nutrient-replete conditions, downstream enzymatic reactions, possibly involving the fatty acid synthase complex or glycerolipid biosynthetic enzymes, appear to be limiting lipid biosynthesis. If the flux through these enzymes were increased, *sta6* may be able to utilize the substantially elevated pool of malonyl CoA. Transcriptomic studies of *C. reinhardtii* have shown a significant increase in the content of acyl transferases such as acyl CoA/diacylglycerol acyltransferase (DGAT) and phospholipid/diacylglycerol acyltransferase, and suggested the involvement of transcription factor NRR1 in potentially regulating the expression of certain diacylglycerol acyltransferase genes and triacylglycerol accumulation (Boyle *et al.*, 2012). The activities of these enzymes in particular may have to be increased to achieve improved lipid yields from malonyl CoA in *sta6*.

In conclusion, our data indicate that, in *C. reinhardtii*, starch biosynthesis plays a critical role in regulating multiple functions, largely through accumulation/utilization of redox and adenylate cofactors. Future research efforts are required to examine mechanisms to effectively leverage the greatly increased malonyl CoA levels for enhanced lipid biosynthesis, which, if successful, may allow higher NADPH re-oxidation rates and restore photosynthetic productivities.

EXPERIMENTAL PROCEDURES

Strains and culture conditions

Chlamydomonas strains CC–4349 *cw15* mt$^-$ (Goodenough 330A, referred to as *cw15*) and *cw15 sta6* (BAFJ5, referred to as *sta6*) (Zabawinski *et al.*, 2001; Wang *et al.*, 2009) were obtained from

the *Chlamydomonas* Resource Center (University of Minnesota, St Paul, MN). *cw15* was chosen as the control strain as it was thought to be the clonal parent to *sta6*. However, during writing of this manuscript, Blaby *et al.* (2013) showed that it is not the original parent, as they do not share the same mating type. However, *cw15* was retained as the control strain in this study because (i) it has an intact starch biosynthetic pathway (Blaby *et al.*, 2013), (ii) like *sta6*, it lacks a cell wall, and (iii) it does not require arginine for growth, making it suitable for autotrophic photosynthetic studies. Liquid cultures were grown in phosphate-buffered Sueoka's high-salt (HS) medium supplemented with 5 mM $NaHCO_3$ and 9.4 mM NH_4Cl (Harris and Stern, 2009). The cultures were maintained on an orbital shaker (100 rpm) under continuous illumination (100 μE m^{-2} sec^{-1} photosynthetically active radiation) at 25°C. For growth rate measurements, flasks were inoculated at a density of approximately 6×10^5 cells ml^{-1}, and cell density was measured daily using a hemocytometer. Growth data were fitted to a Gompertz function (Zwietering *et al.*, 1990) to calculate the specific growth rate and doubling time. For all other characterizations, cells were grown in semi-continuous cultures at a density of 8.8–11 $\times$ 10^6 cells ml^{-1}. For biomass measurements, pre-cultures were grown to approximately 15–20 $\times$ 10^6 cells ml^{-1} and then resuspended at 2.5 $\times$ 10^6 cells ml^{-1} in fresh HS medium. Samples were taken immediately after resuspension (0 h) and at 96 h.

Chlorophyll measurements

Chlorophyll concentration was determined spectrophotometrically by methanol extraction using extinction coefficients from Porra *et al.* (1989).

In vivo measurements of oxygen evolution

Light-saturated OERs were measured using a membrane-covered Clark O_2 electrode (Hansatech, http://hansatech-instruments.com/) at 25°C in HS medium containing 5 mM $NaHCO_3$. Samples were illuminated with red light. Light-dependent respiration was measured within 30 sec after onset of darkness, and subtracted from the light-dependent OER to obtain the gross OER. Appropriate electron acceptors and inhibitors were added directly to the sample chamber. Titration curves for the PSII and PSI electron acceptors 2,5–dichloro-*p*–benzoquinone and *N*–dimethyl-4–nitrosoaniline are shown in Figure S3. Light-dependent respiration was not subtracted when reporting data using artificial electron acceptors.

Relative electron transport rate and non-photochemical measurements

Electron transport rates and NPQ were measured on a pulse-amplitude modulated fluorometer (model FL–3000; Photon Systems Instruments, www.psi.cz/) (Schreiber *et al.*, 1997). Cultures were diluted to 2.5 μg chlorophyll ml^{-1} in HS medium containing 5 mM $NaHCO_3$, and incubated in the dark for 15 min before each experiment. Samples were illuminated for 10 min before a saturating pulse was applied. Electron transport rates and NPQ were calculated using ETR = photosynthetically active radiation $\times$ 0.5 $\times$ 0.84 x Φ_{PSII}, where Φ_{PSII} is equal to $(F'_m - F'_t)/F'_m$ and NPQ = $(F_m/F'_m) - 1$ (Genty *et al.*, 1989).

Fast repetition rate fluorometry measurements

Chlorophyll *a* variable fluorescence yields were measured using a home-built laser fast repetition rate fluorometer (Ananyev and Dismukes, 2005). Whole cells were concentrated to 50 μg ml^{-1} chlorophyll, dark-adapted for 120 sec, then subjected to a train of 50 single-turnover laser flashes (STF) (665 nm, 32 000 μE m^{-2} sec^{-1}) at either 4 Hz (low STF frequency) or 100 Hz (high STF frequency). To maximize the signal to noise ratio, the pulse train was repeated 75 times with 120 sec of dark incubation between consecutive experiments. The variable fluorescence yield was calculated using $F_v = (F_m - F_o)/F_m$ (Maxwell and Johnson, 2000).

Time-resolved O_2 evolution

Time-resolved OERs were measured using a home-built bare platinum electrode controlled by Labview software (Zakrzhevskii *et al.*, 1978), which allows kinetic resolution of the transit time to electron acceptor pools downstream of PSII (PQ, $NADP^+$ and CO_2). Cells were concentrated to 20 μg ml^{-1} chlorophyll, and 8 μl aliquots were loaded onto the 8 mm diameter electrode, dark-incubated for 15 min, and illuminated with red light (400 μE m^{-2} sec^{-1}). The full kinetics of O_2 evolution were recorded over 2 min. The O_2 signals thus generated reflect the size of the electron acceptor pools and the transit times required to fill them (Zakrzhevskii *et al.*, 1978). The O_2 peak associated with reduction of the PQ pool was isolated by subtracting the slower-filling pools by linear extrapolation to the baseline, and the total O_2 evolved was determined from the current using Faraday's law of electrolysis.

Pyridine nucleotide fluorescence kinetics

NAD(P)H fluorescence induction kinetics were measured in whole cells using a home-built instrument similar to one described previously (Mi *et al.*, 2000). A UV-LED (365 nm wavelength) in combination with an optical filter (2 mm UG11, Schott, http://www.schott.com) was used as the excitation light source for NAD(P)H frequency modulated at 100 kHz. A bright red LED (660 nm, Hewlett-Packard, http://www.hp.com/) was used as actinic light. For fluorescence emission detection, we used a low-noise photomultiplier (R2059, Hamamatsu, www.hamamatsu.com) with a maximum sensitivity at 420 nm, protected by a combination of a long-pass filter (KV418, Schott), a short-pass filter (DT-cyan, Optics Blazers, http://opticsbalzers.com/), and a blue/green glass filter (BG39, Schott) to eliminate both the UV-measuring light and chlorophyll fluorescence. An NMR tube with an outer diameter of 5 mm was used as the sample holder, and the detection and excitation pathways were perpendicular. A multifunctional PCI-6036E DAC board (National Instruments, http://www.ni.com/) was used for data acquisition.

Metabolite extraction and analysis

Cultures (8.8-11 $\times$ 10^6 cells ml^{-1}) were quenched in a 60:40 MeOH/water mixture, and centrifuged at 3500 ***g*** for 2 min at 0°C. The supernatant was discarded and the pellet was resuspended in a ice-cold 60:40 methanol/water mixture. The suspension was sonicated for 1 min, and then incubated at −20°C for 20 min. Then the samples were centrifuged for 5 min at 5000 ***g*** at 0°C. The supernatant was vacuum-dried using a Centri Vap benchtop vacuum concentrator (Labconoco, www.labconco.com), and the resulting pellet was resuspended in LC–MS grade water. Samples were injected into an Agilent 6490 QQQ-mass analyzer coupled to an HPLC (Agilent Technologies, www.agilent.com) for metabolite analysis (Kenchappa *et al.*, 2013). Concentrations of each metabolite per cell were calculated using the calibration curve. Fold changes were calculated as a ratio of the concentration of metabolites under LL and HL conditions.

Lipid, glucose and protein analysis

Total lipids were converted to fatty acids for GC-FID analysis as described previously (Radakovits *et al.*, 2012), and analyzed using an Agilent 7890A gas chromatograph and DB5 ms column with flame ionization detection. Total sugar was analyzed using the anthrone assay (Morris, 1948; Meuser *et al.*, 2012). Protein levels were determined using a DC protein assay kit (Bio–Rad, www.bio-rad.com) according to the manufacturer's instructions.

ACKNOWLEDGMENTS

We are grateful to Sabeeha Merchant and Ian Blaby, Department of Chemistry and Biochemistry, UCLA, USA for sharing *cw15* sequencing data. We thank the reviewers for their constructive comments. A.K. was supported by a Benedict Michael Fellowship. D.J.V. was supported by a US National Science Foundation Graduate Research Fellowship (DGE-0937373). This work was funded by Air Force Office of Scientific Research grants FA9550-05-1-0365 and FA9550-14-1-0147, and by Rutgers University.

SUPPORTING INFORMATION

Additional Supporting Information may be found in the online version of this article.

Figure S1. Percentage difference between OER and ETR.

Figure S2. Dark/light/dark induction transients of blue-green fluorescence in *Chlamydomonas reinhardtii*.

Figure S3. Titration curves for 2,4-dichloro-*p*-benzoquinone and *N*-dimethyl-4-nitrosoaniline.

REFERENCES

Ananyev, G. and Dismukes, G.C. (2005) How fast can photosystem II split water? Kinetic performance at high and low frequencies. *Photosynth. Res.* **84**, 355–365.

Ballicora, M.A., Iglesias, A.A. and Preiss, J. (2004) ADP-glucose pyrophosphorylase: a regulatory enzyme for plant starch synthesis. *Photosynth. Res.* **79**, 1–24.

Becker, E.W. (1994) *Microalgae: Biotechnology and Microbiology*. Cambridge: Cambridge Univeristy Press.

Benamotz, A., Tornabene, T.G. and Thomas, W.H. (1985) Chemical profile of selected species of microalgae with emphasis on lipids. *J. Phycol.* **21**, 72–81.

Bennette, N.B., Eng, J.F. and Dismukes, G.C. (2011) An LC-MS-based chemical and analytical method for targeted metabolite quantification in the model cyanobacterium Synechococcus sp. PCC 7002. *Anal. Chem.* **83**, 3808–3816.

Berg, J.M., Tymoczko, J.L. and Stryer, L. (2002) *Biochemistry*. New York: W H Freeman.

Blaby, I.K., Glaesener, A.G., Mettler, T. *et al.* (2013) Systems-level analysis of nitrogen starvation-induced modifications of carbon metabolism in a *Chlamydomonas reinhardtii* starchless mutant. *Plant Cell*, **25**, 4305–4323.

Boyle, N.R., Page, M.D., Liu, B.S. *et al.* (2012) Three acyltransferases and nitrogen-responsive regulator are implicated in nitrogen starvation-induced triacylglycerol accumulation in Chlamydomonas. *J. Biol. Chem.* **287**, 15811–15825.

Caspar, T., Huber, S.C. and Somerville, C. (1985) Alterations in growth, photosynthesis, and respiration in a starchless mutant of *Arabidopsis thaliana* (L.) deficient in chloroplast phosphoglucomutase activity. *Plant Physiol.* **79**, 11–17.

Cerovic, Z.G., Bergher, M., Goulas, Y., Tosti, S. and Moya, I. (1993) Simultaneous measurement of changes in red and blue fluorescence in illuminated isolated-chloroplasts and leaf pieces - the contribution of NADPH to the blue fluorescence signal. *Photosynth. Res.* **36**, 193–204.

Fan, J.L., Yan, C.S., Andre, C., Shanklin, J., Schwender, J. and Xu, C.C. (2012) Oil accumulation is controlled by carbon precursor supply for fatty acid synthesis in *Chlamydomonas reinhardtii*. *Plant Cell Physiol.* **53**, 1380–1390.

Geigenberger, P. (2011) Regulation of starch biosynthesis in response to a fluctuating environment. *Plant Physiol.* **155**, 1566–1577.

Genty, B., Briantais, J.M. and Baker, N.R. (1989) The relationship between the quantum yield of photosynthetic electron-transport and quenching of chlorophyll fluorescence. *Biochim. Biophys. Acta*, **990**, 87–92.

Goodenough, U., Blaby, I., Casero, D. *et al.* (2014) The path to triacylglyceride obesity in the sta6 strain of *Chlamydomonas reinhardtii*. *Eukaryot. Cell*, **13**, 591–613.

Goodson, C., Roth, R., Wang, Z.T. and Goodenough, U. (2011) Structural correlates of cytoplasmic and chloroplast lipid body synthesis in *Chlamydomonas reinhardtii* and stimulation of lipid body production with acetate boost. *Eukaryot. Cell*, **10**, 1592–1606.

Grundel, M., Scheunemann, R., Lockau, W. and Zilliges, Y. (2012) Impaired glycogen synthesis causes metabolic overflow reactions and affects stress responses in the cyanobacterium Synechocystis sp. PCC 6803. *Microbiology*, **158**, 3032–3043.

Guy, R.D., Vanlerberghe, G.C. and Turpin, D.H. (1989) Significance of phosphoenolpyruvate carboxylase during ammonium assimilation: carbon isotope discrimination in photosynthesis and respiration by the N-limited green alga *Selenastrum minutum*. *Plant Physiol.* **89**, 1150–1157.

Harris, E.H. and Stern, D. (2009) *The Chlamydomonas Sourcebook*. Oxford: Academic Press.

Hardie, D. G. and Pan, D. A. (2002) Regulation of fatty acid synthesis and oxidation by the AMP-activated protein kinase. *Biochem. Soc. Trans.*, **30**, 1064–1070.

Johnson, X. and Alric, J. (2012) Interaction between starch breakdown, acetate assimilation, and photosynthetic cyclic electron flow in *Chlamydomonas reinhardtii*. *J. Biol. Chem.* **287**, 26445–26452.

Kenchappa, K.G., Guerra, T., Qian, X., Zhang, S., Bryan, D. and Dismukes, G.C. (2013) Reprogramming the glycolytic pathway for increased hydrogen production in cyanobacteria: metabolic engineering of NAD+-dependent GAPDH. *Energy Environ. Sci.* **6**, 3722–3731.

Kolling, D.R.J., Brown, T.S., Ananyev, G. and Dismukes, G.C. (2009) Photosynthetic oxygen evolution is not reversed at high oxygen pressures: mechanistic consequences for the water-oxidizing complex. *Biochemistry*, **48**, 1381–1389.

Kramer, D.M. and Evans, J.R. (2011) The importance of energy balance in improving photosynthetic productivity. *Plant Physiol.* **155**, 70–78.

Li, Y., Han, D., Hu, G., Dauvillee, D., Sommerfeld, M., Ball, S. and Hu, Q. (2010a) Chlamydomonas starchless mutant defective in ADP-glucose pyrophosphorylase hyper-accumulates triacylglycerol. *Metab. Eng.* **12**, 387–391.

Li, Y., Han, D., Hu, G., Sommerfeld, M. and Hu, Q. (2010b) Inhibition of starch synthesis results in overproduction of lipids in Chlamydomonas reinhardtii. *Biotechnol. Bioeng.* **107**, 258–268.

Ludewig, F., Sonnewald, U., Kauder, F., Heineke, D., Geiger, M., Stitt, M., Muller-Rober, B.T., Gillissen, B., Kuhn, C. and Frommer, W.B. (1998) The role of transient starch in acclimation to elevated atmospheric CO_2. *FEBS Lett.* **429**, 147–151.

Maxwell, K. and Johnson, G.N. (2000) Chlorophyll fluorescence - a practical guide. *J. Exp. Bot.* **51**, 659–668.

Meuser, J.E., D'Adamo, S., Jinkerson, R.E., Mus, F., Yang, W., Ghirardi, M.L., Seibert, M., Grossman, A.R. and Posewitz, M.C. (2012) Genetic disruption of both *Chlamydomonas reinhardtii* [FeFe]-hydrogenases: insight into the role of HYDA2 in H_2 production. *Biochem. Biophys. Res. Commun.* **417**, 704–709.

Mi, H.L., Klughammer, C. and Schreiber, U. (2000) Light-induced dynamic changes of NADPH fluorescence in Synechocystis PCC 6803 and its ndhB-defective mutant M55. *Plant Cell Physiol.* **41**, 1129–1135.

Morris, D.L. (1948) Quantitative determination of carbohydrates with Dreywood's anthrone reagent. *Science*, **107**, 254–255.

Porra, R.J., Thompson, W.A. and Kriedemann, P.E. (1989) Determination of accurate extinction coefficients and simultaneous-equations for assaying chlorophyll-a and chlorophyll-b extracted with 4 different solvents - verification of the concentration of chlorophyll standards by atomic-absorption spectroscopy. *Biochim. Biophys. Acta*, **975**, 384–394.

Radakovits, R., Jinkerson, R.E., Darzins, A. and Posewitz, M.C. (2010) Genetic engineering of algae for enhanced biofuel production. *Eukaryot. Cell*, **9**, 486–501.

Radakovits, R., Jinkerson, R.E., Fuerstenberg, S.I., Tae, H., Settlage, R.E., Boore, J.L. and Posewitz, M.C. (2012) Draft genome sequence and genetic transformation of the oleaginous alga *Nannochloropis gaditana*. *Nat. Commun.* **3**, 686.

Rochaix, J.D. (2011) Regulation of photosynthetic electron transport. *Biochim. Biophys. Acta*, **1807**, 375–383.

Schreiber, U., Gademann, R., Ralph, P.J. and Larkum, A.W.D. (1997) Assessment of photosynthetic performance of *Prochloron* in *Lissoclinum patella* in hospite by chlorophyll fluorescence measurements. *Plant Cell Physiol.* **38**, 945–951.

Sharkey, T.D., Stitt, M., Heineke, D., Gerhardt, R., Raschke, K. and Heldt, H.W. (1986) Limitation of photosynthesis by carbon metabolism. 2. O_2-Insensitive CO_2 uptake results from limitation of triose phosphate utilization. *Plant Physiol.* **81**, 1123–1129.

Siaut, M., Cuine, S., Cagnon, C. *et al.* (2011) Oil accumulation in the model green alga Chlamydomonas reinhardtii: characterization, variability between common laboratory strains and relationship with starch reserves. *BMC Biotechnol.* **11**, 7.

Stitt, M. and Quick, P. (1989) Photosynthetic carbon partitioning - its regulation and possibilities for manipulation. *Physiol. Plant.* **77**, 633–641.

Storer, A.C. and Cornish-Bowden, A. (1976) Concentration of MgATP2- and other ions in solution. Calculation of the true concentrations of species present in mixtures of associating ions. *Biochem. J.*, **159**, 1–5.

Subramanian, S., Barry, A.N., Pieris, S. and Sayre, R.T. (2013) Comparative energetics and kinetics of autotrophic lipid and starch metabolism in chlorophytic microalgae: implications for biomass and biofuel production. *Biotechnol. Biofuels*, **6**, 150.

Sun, J.D., Okita, T.W. and Edwards, G.E. (1999) Modification of carbon partitioning, photosynthetic capacity, and O_2 sensitivity in Arabidopsis plants with low ADP-glucose pyrophosphorylase activity. *Plant Physiol.* **119**, 267–276.

Suzuki, E., Ohkawa, H., Moriya, K., Matsubara, T., Nagaike, Y., Iwasaki, I., Fujiwara, S., Tsuzuki, M. and Nakamura, Y. (2010) Carbohydrate metabolism in mutants of the cyanobacterium *Synechococcus elongatus* PCC 7942 defective in glycogen synthesis. *Appl. Environ. Microbiol.* **76**, 3153–3159.

Vinyard, D.J., Zachary, C.E., Ananyev, G. and Dismukes, G.C. (2013) Thermodynamically accurate modeling of the catalytic cycle of photosynthetic oxygen evolution: a mathematical solution to asymmetric Markov chains. *Biochim. Biophys. Acta*, **1827**, 861–868.

Wang, Z.T., Ullrich, N., Joo, S., Waffenschmidt, S. and Goodenough, U. (2009) Algal lipid bodies: stress induction, purification, and biochemical characterization in wild-type and starchless Chlamydomonas reinhardtii. *Eukaryot. Cell*, **8**, 1856–1868.

Weise, S.E., van Wijk, K.J. and Sharkey, T.D. (2011) The role of transitory starch in C-3, CAM, and C-4 metabolism and opportunities for engineering leaf starch accumulation. *J. Exp. Bot.* **62**, 3109–3118.

Work, V.H., Radakovits, R., Jinkerson, R.E., Meuser, J.E., Elliott, L.G., Vinyard, D.J., Laurens, L.M., Dismukes, G.C. and Posewitz, M.C. (2010) Increased lipid accumulation in the *Chlamydomonas reinhardtii* sta7-10 starchless isoamylase mutant and increased carbohydrate synthesis in complemented strains. *Eukaryot. Cell*, **9**, 1251–1261.

Zabawinski, C., Van Den Koornhuyse, N., D'Hulst, C., Schlichting, R., Giersch, C., Delrue, B., Lacroix, J.M., Preiss, J. and Ball, S. (2001) Starchless mutants of *Chlamydomonas reinhardtii* lack the small subunit of a heterotetrameric ADP-glucose pyrophosphorylase. *J. Bacteriol.* **183**, 1069–1077.

Zakrzhevskii, D.A., Ananyev, G.A. and Gerts, S.M. (1978) Kinetics of oxygen evolution by Chlorella cells ducing the initial period of illumination. *Soviet Plant Physiol.* **25**, 653–658.

Zwietering, M.H., Jongenburger, I., Rombouts, F.M. and Vantriet, K. (1990) Modeling of the bacterial-growth curve. *Appl. Environ. Microbiol.* **56**, 1875–1881.